

Nearly flat Chern band in periodically strained monolayer and bilayer graphene

Xiaohan Wan,^{1,2} Siddhartha Sarkar,² Kai Sun,^{2,*} and Shi-Zeng Lin^{1,3,†}

¹Theoretical Division, T-4 and CNLS, Los Alamos National Laboratory (LANL), Los Alamos, New Mexico 87545, USA

²Department of Physics, University of Michigan, Ann Arbor, Michigan 48109, USA

³Center for Integrated Nanotechnologies (CINT), Los Alamos National Laboratory (LANL), Los Alamos, New Mexico 87545, USA



(Received 20 February 2023; revised 4 August 2023; accepted 12 September 2023; published 20 September 2023)

The flat band is a key ingredient for the realization of interesting quantum states for functionalities. In this paper, we investigate the conditions for the flat band in both monolayer and bilayer graphene under periodic strain. We find topological nearly flat bands with homogeneous distribution of Berry curvature in both systems. The quantum metric of the nearly flat band closely resembles that for Landau levels. For monolayer graphene, the strain field can be regarded as an effective gauge field, while for Bernal-stacked (*AB*-stacked) bilayer graphene, its role is beyond the description of a gauge field. We also provide an understanding of the origin of the nearly flat band in monolayer graphene in terms of the Jackiw-Rebbi model for Dirac fermions with sign-changing mass. In this paper, we suggest strained graphene as a promising platform for strongly correlated quantum states.

DOI: [10.1103/PhysRevB.108.125129](https://doi.org/10.1103/PhysRevB.108.125129)

I. INTRODUCTION

Electron correlation is at the center of condensed matter physics research and is the driving mechanism for a variety of quantum states of matter. There are several known routes to tune the system into a strongly correlated region. In a Landau Fermi liquid, the Coulomb interaction can dominate the electron kinetic energy by tuning the density of the electron to the dilute region. The strongly correlated region can also be achieved using localized electron orbitals, such as electrons in the *d* or *f* shell. This is illustrated in two paradigmatic models in condensed matter physics: the Hubbard model and the Anderson lattice model for *f* electrons. In these correlated systems, the physics connects to the atomic limit adiabatically. For instance, by using more and more localized electron orbitals, the overlap of the orbital wave function between neighboring sites can be progressively reduced to approach the atomic limit. Therefore, the narrow electron band in these systems generally has a trivial band topology. Another route is to take advantage of the interference effect of the electron wave function when electrons hop in the lattice. For certain lattices, such as Lieb and Kagome lattices, there exists an exactly flat band. The condition for the existence of exactly flat band was derived by Lieb [1]. Nearly flat bands have been achieved in carefully designed Hamiltonians [2–4]. Recently, moiré superlattices have emerged as an exciting platform for attaining a nearly flat band through the interference effect of the electron wave function [5]. A moiré superlattice appears when two incommensurate periodic structures are superposed together. This can be achieved by twisting a two-monolayer material or by placing a layer of two-dimensional material on top of another material with a different lattice parameter. As a

result of incommensuration, a superlattice with much longer lattice periodicity arises. (Rigorously speaking, the superlattice is generally not periodic, but at the low-energy scale, the incommensuration effect is not important, and the system can be treated as a periodic lattice.) Here, we emphasize that the narrow band in the moiré superlattice is not merely due to the reduced energy scale for a small Brillouin zone in the superlattice with a long period. This can be seen by checking the ratio between the band gap and the bandwidth, which can be large under certain conditions. The single particle band is generally not exactly flat in a moiré superlattice [5], except for certain special parameters [6]. Nevertheless, these nearly flat bands are sufficient to stabilize a plethora of correlated states, such as superconductivity, correlated insulating states, and Wigner crystals [7–32].

The third route is to apply a magnetic field which quenches the kinetic energy of electrons in the plane perpendicular to the magnetic field. Electrons occupy the Landau levels, which are exactly flat in the clean bulk. Moreover, the system is topological, as evidenced by an integer quantized Hall conductance. The Landau levels have other unique properties, such as saturation of the trace condition. These properties make Landau-level systems important for stabilizing exotic quantum states, such as the fractional quantum Hall state and many other states with nontrivial topological order.

It is natural to seek similar Landau-level physics in materials but without an external magnetic field. This is indeed possible in systems where strain can be regarded as a pseudomagnetic field. This idea has been explored extensively in the context of graphene [33], and the formation of Landau levels has also been observed in experiments [34]. Unlike the physical magnetic field, the strain does not break the time-reversal symmetry. This means that the pseudomagnetic field must be opposite for Dirac fermions in two different valleys in graphene. The pseudomagnetic field can also stabilize a nontrivial topological phase in graphene, as was recently

*sunkai@umich.edu

†szl@lanl.gov

demonstrated in Ref. [35]. Experimentally, the narrow band in graphene under periodic strain was reported [36] and was investigated theoretically in Refs. [37–39]. Therefore, strain engineering represents an important direction to achieve flat bands, parallel to the efforts to identify materials with intrinsic flat bands [40].

In this paper, we study the occurrence and condition of a nearly flat band in both monolayer and bilayer graphene under periodic strain. We identify nearly flat bands with a nonzero valley-resolved Chern number in monolayer graphene. This flat band can be understood based on the Jackiw-Rebbi (JR) zero mode in a $(1+1)$ -dimensional $[(1+1)\text{D}]$ Dirac fermion with spatially varying mass. We then go beyond the simple Dirac fermion with winding number 1 to a Dirac fermion with winding number 2 stabilized in bilayer graphene. For Dirac fermions in graphene, the strain field can only shift the position of the Dirac cone before the Dirac cone annihilates with the other Dirac fermion in the opposite valley. In this case, the strain can be regarded as a pseudomagnetic field. In bilayer graphene, in addition to the shift of the position of the Dirac cone, the Dirac fermion with winding number 2 can split into two Dirac fermions with winding number 1 or other combinations such as 3 Dirac cones with winding 1 and one cone with winding -1 . In this case, the strain field decomposes into two separate sectors: symmetric and antisymmetric (under inversion). In analogy to strain in single-layer systems, the symmetric sector results in an effective gauge field. In contrast, the antisymmetric sector provides a distinctive coupling between strain and electronic degrees of freedom, which can no longer be treated as an effective gauge field, and results in an alternative family of moiré systems. We will show the appearance of nearly flat bands with almost ideal quantum geometry as Landau levels in monolayer and bilayer graphene.

The remainder of the paper is organized as follows. In Sec. II, we review the treatment of strain as a pseudogauge field in monolayer graphene. In Sec. III, we present results of a nearly flat band in monolayer graphene. In Sec. IV, we turn to the flat band in periodic strained bilayer graphene. In Sec. V, we provide an understanding of the occurrence of flat bands in strained monolayer graphene from the perspective of the JR model. We end the paper with a brief discussion and conclusions in Sec. VI.

II. STRAIN

Here, we briefly review how the strain field can be modeled as a pseudomagnetic field in graphene. The valley-projected Hamiltonian of monolayer graphene around K_+ is

$$H_{K_+} = \frac{3}{2}at \begin{pmatrix} 0 & q_x + iq_y \\ q_x - iq_y & 0 \end{pmatrix} = \frac{3}{2}at \begin{pmatrix} 0 & -2i\partial_z \\ -2i\partial_z & 0 \end{pmatrix}, \quad (1)$$

where $\partial_z = \frac{1}{2}(\partial_x - i\partial_y)$, $\partial_{\bar{z}} = \frac{1}{2}(\partial_x + i\partial_y)$, a is the bond length of graphene, and t is the nearest-neighbor hopping strength. After we apply a deformation field \vec{u} to monolayer graphene, the hopping strengths along $\vec{\delta}_1$, $\vec{\delta}_2$, and $\vec{\delta}_3$ (as shown in Fig. 1) are modulated by the strain field. Denote the hopping

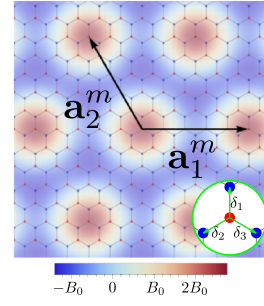


FIG. 1. Schematic view of periodically strained graphene. $\mathbf{a}_1^m = \sqrt{3}N_a a(1, 0)$ and $\mathbf{a}_2^m = \sqrt{3}N_a a(-\frac{1}{2}, \frac{\sqrt{3}}{2})$ are the superlattice lattice vectors. The color map is of the pseudomagnetic field defined in Eq. (10).

strengths along $\vec{\delta}_1$, $\vec{\delta}_2$, and $\vec{\delta}_3$ as t_1 , t_2 , and t_3 , respectively. Then the Hamiltonian is modified as (we use $\hbar = e = c = 1$)

$$H_{K_+} = \frac{3}{2}at \begin{bmatrix} 0 & -2i\partial_z + e(A_x + iA_y) \\ -2i\partial_z + e(A_x - iA_y) & 0 \end{bmatrix}, \quad (2)$$

where $ev_F A_x = \frac{1}{2}(\delta t_2 + \delta t_3 - 2\delta t_1)$, $ev_F A_y = \frac{\sqrt{3}}{2}(\delta t_3 - \delta t_2)$, and $v_F = \frac{3}{2}at$. The relationship between δt_i and the strain tensor u_{ij} is

$$\begin{aligned} t_i &= t + \frac{\partial t}{\partial a} \delta a \\ &= t + \frac{\partial \ln t}{\partial \ln a} \frac{t}{a} \hat{\delta}_i \cdot [\vec{u}_B(\vec{R}_A + \vec{\delta}_i) - \vec{u}_A(\vec{R}_A)], \end{aligned} \quad (3)$$

In the long-wavelength limit,

$$\vec{u}_B(\vec{R}_A + \vec{\delta}_i) - \vec{u}_A(\vec{R}_A) = \kappa(\vec{\delta}_i \cdot \nabla) \vec{u}, \quad (4)$$

where κ is the reduction factor [41]. Then

$$t_i = t + \kappa \frac{\partial \ln t}{\partial \ln a} \frac{t}{a^2} \vec{\delta}_i \cdot (\vec{\delta}_i \cdot \nabla) \vec{u}. \quad (5)$$

Defining $\beta = -\frac{\partial \ln t}{\partial \ln a}$, which measures how the bonds respond to being deformed, we have

$$t_i = t - \frac{\kappa \beta t}{a^2} \vec{\delta}_i \cdot (\vec{\delta}_i \cdot \nabla) \vec{u}. \quad (6)$$

Plugging $\vec{\delta}_1 = (0, a)$, $\vec{\delta}_2 = (-\frac{\sqrt{3}a}{2}, -\frac{a}{2})$, and $\vec{\delta}_3 = (\frac{\sqrt{3}a}{2}, -\frac{a}{2})$ into the above equation, we obtain

$$\delta t_1 = -\beta t \kappa u_{yy}, \quad (7)$$

$$\delta t_2 = -\beta t \kappa \left(\frac{3}{4} u_{xx} + \frac{1}{4} u_{yy} + \frac{\sqrt{3}}{2} u_{xy} \right), \quad (8)$$

$$\delta t_3 = -\beta t \kappa \left(\frac{3}{4} u_{xx} + \frac{1}{4} u_{yy} - \frac{\sqrt{3}}{2} u_{xy} \right). \quad (9)$$

Then we have $A_x = -\frac{\beta \kappa}{2ea}(u_{xx} - u_{yy})$ and $A_y = 2\frac{\beta \kappa}{2ea} u_{xy}$.

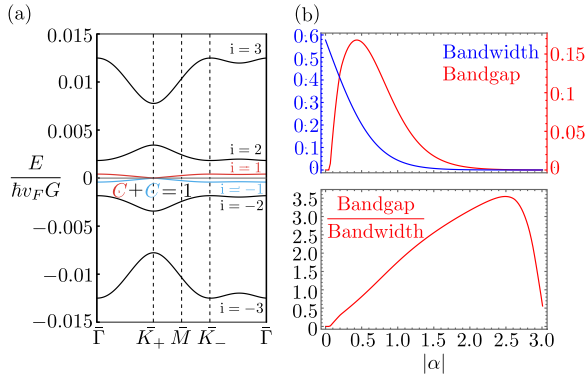


FIG. 2. Topological flat band in buckled monolayer graphene. (a) Band structure at $\alpha = -2.22817$. Blue line corresponds to band 1, and red line corresponds to band -1 . Together, they have valley Chern number 1. (b) Bandwidth (blue line), band gap (red line in the top panel), ratio between band gap and bandwidth (red line in the bottom panel) as a function of $|\alpha|$, respectively. Band gap is the gap between the middle two bands and the band 2, bandwidth is of band -1 or 1. Here, band index i means the i th band counting from the charge neutrality point, as shown in (a).

III. NEARLY FLAT BAND IN MONOLAYER GRAPHENE

We set $\delta t_i/t = \delta t \sin(\vec{G}_i \cdot \vec{r})$, where $\vec{G}_1 = \frac{4\pi}{3Na}(0, 1)$, $\vec{G}_{2,3} = \frac{4\pi}{3Na}(\mp \frac{\sqrt{3}}{2}, -\frac{1}{2})$ are reciprocal lattice vectors. The pseudomagnetic field is

$$\vec{B}(\vec{r}) = B_0 \sum_{i=1}^3 \cos(\vec{G}_i \cdot \vec{r}) \hat{z}, \quad (10)$$

where $B_0 = \frac{4\pi t \delta t}{3ev_F N_n a}$. We define the normalized δt as $\alpha = \frac{\delta t}{(3/2)aG}$, where $G = \frac{4\pi}{3Na}$ is the magnitude of the reciprocal lattice vector. We obtain two nearly flat bands near the charge neutrality point when $\delta t = -0.2$ and $N_n = 70$, which corresponds to $\alpha = -2.22817$, as shown in Fig. 2(a). Adding a $m_0 \sigma_z$ term and setting $m_0 = 0.001$, we get two separated flat bands. The valley Chern number is 1 for the bottom flat band and 0 for the top flat band. Before adding the $m_0 \sigma_z$ term, the ratio between the band gap and the bandwidth of band 1/(-1) is ~ 3 , as shown in Fig. 2(b). Here, band index i means the i th band counting from the charge neutrality point. After adding the $m_0 \sigma_z$ term, the ratio between band gap [the band gap is

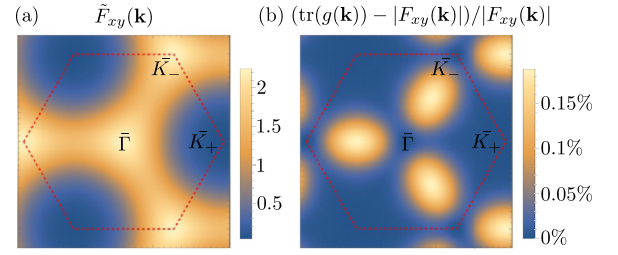


FIG. 3. (a) Berry curvature distribution of the topological band in monolayer strained graphene, where $\tilde{F}_{xy}(\mathbf{k}) = F_{xy}(\mathbf{k})/\tilde{F}_{xy}$. (b) Violation of the trace condition of the topological flat band. Here, we choose $\alpha = -2.22817$ and $m_0 = 0.001$.

between the band 1(-1) and 2(-2) for the top(bottom) band] and bandwidth of the top(bottom) are the same and ~ 18.3 .

In addition to the band dispersion, we further characterize the bands using the Fubini-Study metric $g_{ab}(\mathbf{k})$ and the Berry curvature $F_{xy}(\mathbf{k})$, which are given by

$$g_{ab}(\mathbf{k}) = \Re[\eta_{ab}(\mathbf{k})], \quad F_{xy}(\mathbf{k}) = -2\Im[\eta_{xy}(\mathbf{k})], \quad (11)$$

where

$$\eta_{ab}(\mathbf{k}) = \frac{\langle \partial_a u_{\mathbf{k}} | \partial_b u_{\mathbf{k}} \rangle}{\|u_{\mathbf{k}}\|^2} - \frac{\langle \partial_a u_{\mathbf{k}} | u_{\mathbf{k}} \rangle \langle u_{\mathbf{k}} | \partial_b u_{\mathbf{k}} \rangle}{\|u_{\mathbf{k}}\|^4},$$

where $u_{\mathbf{k}}(\mathbf{r})$ is the periodic part of the Bloch function, $\partial_a \equiv \partial_{k_a}$, and $\|u_{\mathbf{k}}\|^2 = \langle u_{\mathbf{k}} | u_{\mathbf{k}} \rangle$. In analogy to the Landau-level physics, the ideal candidate for the realization of fractional Chern insulators and other correlated topological states should have an ideal quantum metric, i.e., satisfying the trace condition $\text{tr}[g(\mathbf{k})] = |F_{xy}(\mathbf{k})|$, and a very uniform Berry curvature. To quantify the nonuniformity of the Berry curvature, we plot the Berry curvature distribution of the bottom band in Fig. 3(a). The ratio between the root-mean-square deviation of the Berry curvature and its average value $\Delta F_{xy}/\tilde{F}_{xy} = 0.576179$. We also plot the violation of the trace condition quantified by $\{\text{tr}[g(\mathbf{k})] - |F_{xy}(\mathbf{k})|\}/|F_{xy}(\mathbf{k})|^{-1}$ in Fig. 3(b). We find that the deviation of $\text{tr}[g(\mathbf{k})]$ from $|F_{xy}(\mathbf{k})|$ is very small ($< 0.18\%$) in the entire Brillouin zone for the chosen value of $\alpha = -2.22817$.

IV. NEARLY FLAT BANDS IN BILAYER GRAPHENE

Here, we consider Bernal-stacked (AB -stacked) bilayer graphene, which hosts Dirac fermions with winding number 2. The generic valley projected Hamiltonian of the strained bilayer graphene is

$$H_{K_+} = \frac{3}{2}at \begin{pmatrix} 0 & -2i\partial_z + e\tilde{A}_1 & 0 & 0 \\ -2i\partial_z + e\tilde{A}_1^* & 0 & \frac{2\gamma}{3at} & 0 \\ 0 & \frac{2\gamma}{3at} & 0 & -2i\partial_z + e\tilde{A}_2 \\ 0 & 0 & -2i\partial_z + e\tilde{A}_2^* & 0 \end{pmatrix}, \quad (12)$$

where $\tilde{A}_1 = A_{1x} + iA_{1y}$, $\tilde{A}_2 = A_{2x} + iA_{2y}$, and γ is the interlayer hopping strength. In the following calculation, we set $\gamma = 0.1t$. We define the symmetric and antisymmetric fields $\tilde{A}^{(+)} = \frac{\tilde{A}_1 + \tilde{A}_2}{2}$ and $\tilde{A}^{(-)} = \frac{\tilde{A}_1 - \tilde{A}_2}{2}$, respectively. In

Bernal-stacked bilayer graphene, the aligned top layer A sublattice and the bottom layer B sublattice hybridize strongly and are responsible for the formation of bands away from zero energy. Therefore, we can project out these two interlayer

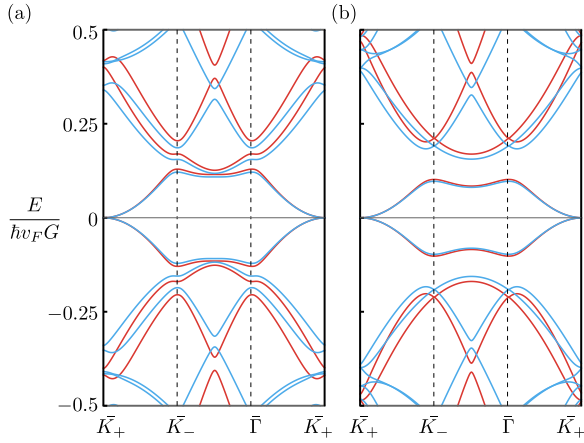


FIG. 4. (a) 4×4 (blue line) and 2×2 (red line) band structure for symmetric strained bilayer graphene with $\alpha = 0.159155$. (b) 4×4 (blue line) and 2×2 (red line) band structure for antisymmetric strained bilayer graphene with $\alpha = -0.159155$.

aligned sublattices and derive a low-energy Hamiltonian for the unaligned sublattice. Then the 2×2 effective Hamiltonian of Eq. (12) is

$$H_{\text{eff}} = \frac{9a^2t^2}{4\gamma} \begin{pmatrix} 0 & H_{12} \\ H_{12}^* & 0 \end{pmatrix}, \quad (13)$$

where

$$\begin{aligned} H_{12} &= -[-2i\partial_z + e\tilde{A}^{(+)} + e\tilde{A}^{(-)}][-2i\partial_z + e\tilde{A}^{(+)} - e\tilde{A}^{(-)}] \\ &= 4\partial_z^2 - e^2[\tilde{A}^{(+)}]^2 + e^2[\tilde{A}^{(-)}]^2 + 4ei\tilde{A}^{(+)}\partial_z \\ &\quad + 2ei\partial_z\tilde{A}^{(+)} - 2ei\partial_z\tilde{A}^{(-)}. \end{aligned} \quad (14)$$

It is evident from Eq. (13) that, when the strain field is symmetric with $\tilde{A}^{(-)} = 0$ (i.e., the same for both layers), it acts as a gauge field $[-2i\partial_z \rightarrow -2i\partial_z + e\tilde{A}^{(+)}]$. However, the antisymmetric part of the strain field $\tilde{A}^{(-)}$ cannot be treated as an effective gauge field. Note that the symmetric and antisymmetric components of the strain field \tilde{A} do not mix. In the following, we discuss these two cases separately.

A. Bilayer graphene with symmetric strain for two layers

When the two layers have the same strain, $\tilde{A}^{(-)} = 0$. Setting $\tilde{A}^{(+)} = A_x + iA_y$:

$$A_x = \frac{-1}{ev_F}t\delta t \left[\sin(\vec{G}_1 \cdot \vec{r}) - \frac{1}{2} \sin(\vec{G}_2 \cdot \vec{r}) - \frac{1}{2} \sin(\vec{G}_3 \cdot \vec{r}) \right], \quad (15)$$

$$A_y = \frac{-1}{ev_F}t\delta t \left[\frac{\sqrt{3}}{2} \sin(\vec{G}_2 \cdot \vec{r}) - \frac{\sqrt{3}}{2} \sin(\vec{G}_3 \cdot \vec{r}) \right]. \quad (16)$$

We plot the band structure of the 4×4 Hamiltonian and the 2×2 effective Hamiltonian and find that they agree well near the charge neutrality point when the strength of the strain field is small, as shown for $\alpha = 0.159155$ in Fig. 4(a). Because $\rho(C_2T)H_{\text{eff}}^*(\mathbf{r}, \delta t)\rho(C_2T)^\dagger = H_{\text{eff}}(C_2\mathbf{r}, -\delta t)$, the band structure for δt and $-\delta t$ are the same. Both $\delta t > 0$ and $\delta t < 0$ lead to a nonzero band gap between the middle two bands and the other bands. Before adding any σ_z term, band 2 already has

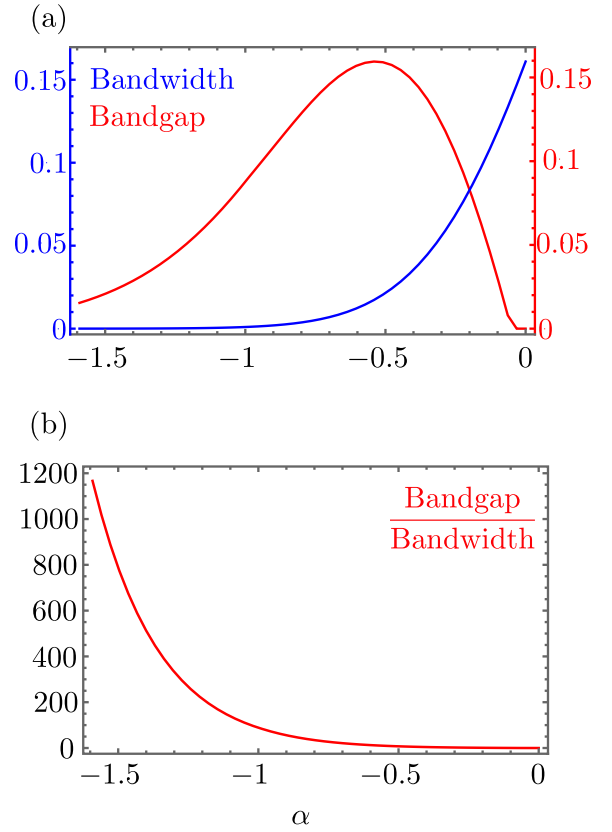


FIG. 5. Band gap and bandwidth plot of antisymmetric strained bilayer graphene. (a) Bandwidth (blue line) of band 1/(-1), band gap (red line) between band 1(-1) and band 2(-2) and (b) the ratio between band gap and bandwidth (red line) as a function of $|\alpha|$. The plot is from the 4×4 Hamiltonian. The normalized δt is defined as $\alpha = \frac{\delta t}{\frac{3}{2}aG}$. The energy is shown in units of $\hbar v_F G$.

a valley Chern number $+2/-2$, depending on the sign of δt . When $\delta t < 0$, after adding the σ_z term, bands $-1, 1$, and 2 have valley Chern numbers $-2, 0$, and 2 , respectively. When $\delta t > 0$, after adding the σ_z term, the bands $-1, 1$, and 2 have valley Chern numbers $0, 2$, and -2 , respectively.

B. Bilayer graphene with opposite strain for two layers

When the two layers have the opposite strain, we have $\tilde{A}^{(+)} = 0$. We set $\tilde{A}^{(-)} = A_x + iA_y$, where A_x and A_y are the same as in Eqs. (15) and (16). Unlike the case of symmetric strain, for antisymmetric strain, positive and negative δt lead to different behavior. When $\delta t > 0$, the middle two bands are gapless. When $\delta t < 0$, the two middle bands are separated from others, and the flatness of the two middle bands increases monotonically as we increase $|\alpha|$, as shown in Fig. 5.

We calculate the valley Chern number of the middle two bands after adding the σ_z term; the top flat band has valley Chern number -1 and the lower one $+1$. We plot the Berry curvature distribution and the violation of the trace condition $\{\text{tr}[g(\mathbf{k})] - |F_{xy}(\mathbf{k})|\}|F_{xy}(\mathbf{k})|^{-1}$ of the bottom band at $\alpha = -1.59155$. The ratio between band gap and bandwidth is >1000 after adding σ_z , and we have an ideal quantum geometry, as shown in Fig. 6(b). Here, $|\psi_{K_+}(\mathbf{r}_0 = \mathbf{0})|$ decreases exponentially as a function of $|\alpha|$, as shown in

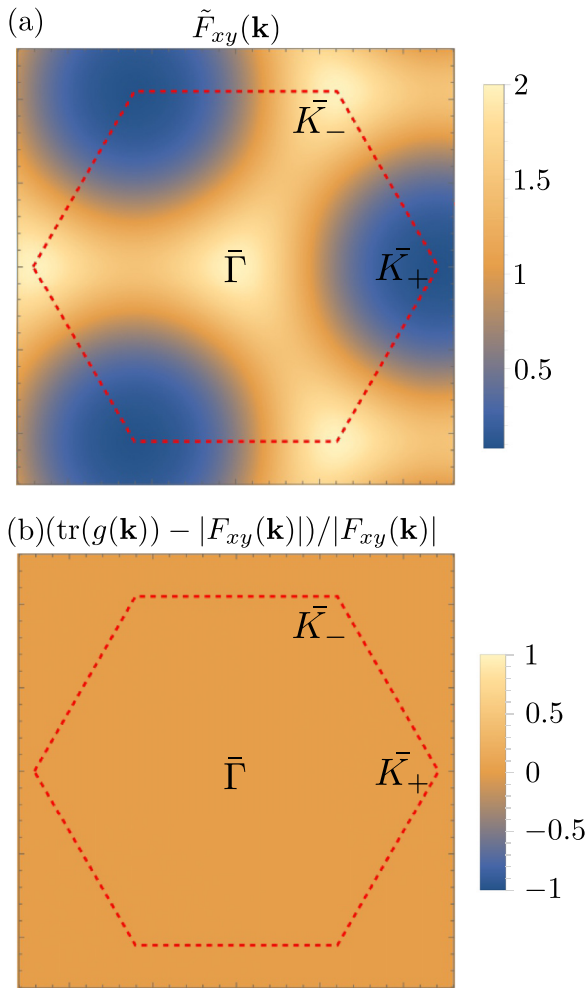


FIG. 6. (a) Distribution of the Berry curvature. (b) Violation of the trace condition of the lower topological flat band for antisymmetric strained bilayer graphene at $\alpha = -1.59155$ and $m_0 = 0.0001$. The plots are from the 4×4 Hamiltonian. m_0 is amplitude of $\mathbb{1} \otimes \sigma_z$ term.

Fig. 7. When $|\alpha|$ is large, $|\psi_{\bar{K}_+}(\mathbf{r}_0 = \mathbf{0})|$ is very close to 0, suggesting that the wave function of the topological flat band is close to a trial wave function $\psi_{\mathbf{k}}(\mathbf{r}) = f_{\mathbf{k}}(z)\psi_{\bar{K}_+}(\mathbf{r})$, where $\psi_{\bar{K}_+}(\mathbf{r})$ has a zero at $\mathbf{r} = \mathbf{0}$. The periodic part of this trial wave function is holomorphic in k , which gives rise to the perfect quantum geometry of the band. As shown in Fig. 8, the decay rate of $\{[\text{tr}[g(\mathbf{k})] - |F_{xy}(\mathbf{k})|]/|F_{xy}(\mathbf{k})|\}^{-1}$ as a function of $|\alpha|$ for the bilayer is much faster than that of the monolayer, suggesting that the quantum geometry of the bilayer topological flat band is closer to the ideal quantum geometry than the monolayer topological flat band with the same α .

V. CONNECTION TO THE JR ZERO MODE

For Dirac fermions coupled to a gauge field, it was proved that there exist zero modes whose number is the same as the number of total flux minus one in the system [42]. Whereas this applies even to the situation where the magnetic field is not uniform in space, it does not apply to the case where the net magnetic flux is zero. In strained graphene systems, the net magnetic flux is zero, so the calculations of Ref. [42] are

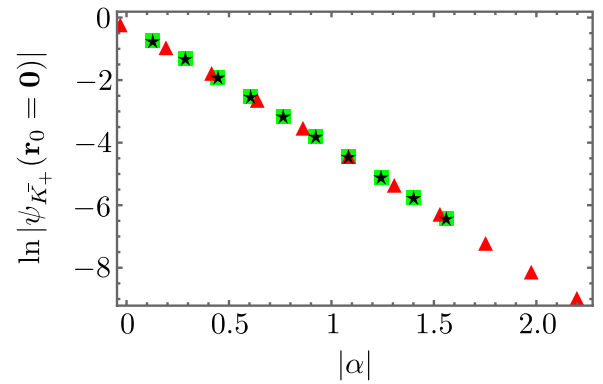


FIG. 7. Plot of $\ln |\psi_{\bar{K}_+}(\mathbf{r}_0 = \mathbf{0})|$ as a function of $|\alpha|$ for monolayer, bilayer 4×4 Hamiltonian, and bilayer 2×2 effective Hamiltonian. Red triangle is for monolayer, Black star is for bilayer 2×2 , Green square is for bilayer 4×4 .

no longer applicable. Instead, the nearly flat band in the monolayer graphene system can be understood from the perspective of the zero mode of the Dirac fermion in $(1+1)\text{D}$ with a sign-changing mass term, the JR zero mode [43]. To build intuition, we first show that zero modes in graphene under a uniform magnetic field (zeroth Landau level) can be captured with the JR method and how it can be extended to capture partially flat bands in graphene under a (pseudo)magnetic field that varies only in one spatial direction. Then we show details of the JR model in strained monolayer graphene.

For a Dirac Hamiltonian in $(1+1)\text{D}$, $\mathcal{H}(x) = -i\partial_x\sigma_x + m(x)\sigma_y$, with a sign-changing mass term, i.e., $m(x \geq 0) \geq 0$ and $m(x < 0) < 0$, it supports a massless fermionic mode localized at the domain wall $x = 0$. For zeroth Landau level in graphene, we take the gauge $A_y = B_z x$ and $A_x = 0$, such that the momentum k_y in the y direction is a good quantum number. For each k_y , the Dirac Hamiltonian in one valley K becomes $\mathcal{H}(x)_K = -i\partial_x\sigma_x + (k_y - B_z x)\sigma_y$ which is exactly the $(1+1)\text{D}$ Dirac Hamiltonian with a spatially dependent mass term $m(x) = k_y - B_z x$. For each k_y , there exists a JR zero

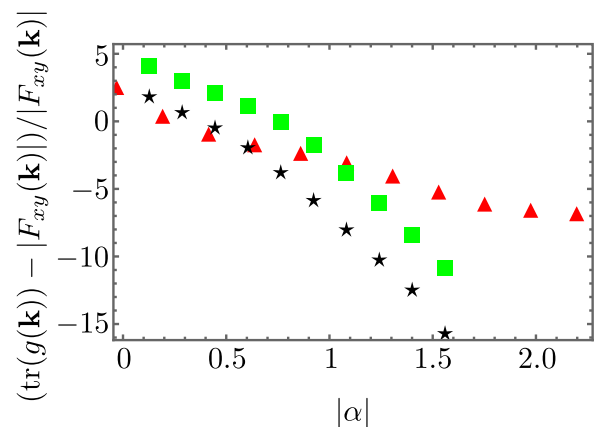


FIG. 8. Trace condition violation for monolayer and bilayer 4×4 and 2×2 effective Hamiltonian as a function of $|\alpha|$ at a fixed k point. We choose the middle point between $\bar{\Gamma}$ and \bar{K}_- for the monolayer case. We choose $\bar{\Gamma}$ for the bilayer case. Red triangle is for monolayer. Black star is for bilayer 2×2 . Green square is for bilayer 4×4 .

mode at $x_{JR} = k_y/B_z$. The degeneracy of the zeroth Landau level is equal to the number of allowed k_y , which equals $N_y = L_x/x_{JR} = L_x L_y B_z / (2\pi) = \Phi / \Phi_0$, where L_x and L_y are the linear system sizes, and we take k_y to be discretized in a step of $2\pi/L_y$. This reproduces the well-known results that the degeneracy of the zeroth Landau level is the same as the number of flux in units of flux quantum. In the presence of an electric field E_y along the y direction, $k_y = E_y t$ from the semiclassical equation of motion for electrons. After one period, the position of the zero mode in the x direction is exactly shifted by one period, which corresponds to quantized electrical Hall conductance $\sigma_{xy} = 1/2\pi$. Therefore, the zeroth Landau level is topological. The JR model reproduces the well-known facts about the zeroth Landau level of Dirac fermions in $(2 + 1)D$.

However, for a gauge field which corresponds to a uniform magnetic field, the associated strain field diverges at large distances and thus cannot be realized physically. To avoid divergence in the strain field, we choose a sinusoidal vector potential varying only in the x direction, which can be realized using the deformation field $u_y \propto \sin(\frac{2\pi}{N_n} \frac{x}{\sqrt{3}a})$ and $u_x = 0$. Note that there are infinitely many possible strain field configurations that give the same pseudomagnetic field. The Hamiltonian is

$$\mathcal{H}(x, k_y) = v_F \{-i\partial_x \sigma_x + [k_y + eA_y(x)]\sigma_y\}, \quad (17)$$

where we take $A_y(x) = \frac{t}{ev_F} \delta t \cos(\frac{2\pi}{N_n} \frac{x}{\sqrt{3}a})$. In the region where $k_y < |\frac{t\delta t}{v_F}|$, there exists a quasizero mode localized in the region when $k_y + eA_y(x)$ changes sign. Here, quasizero means that these localized modes generally hybridize, which lifts these modes away from zero energy. The degree of hybridization depends on the ratio between the spread of the wave function and the separation of the zeros of $k_y + eA_y(x)$. As k_y approaches $|\frac{t\delta t}{v_F}|$, the hybridization of the localized mode becomes stronger, and the energy of the modes starts to deviate from zero energy. As a consequence, the band is nearly flat only in a certain range of k_y , as illustrated in Fig. 9. The partially flat band result is consistent with the tight-binding model result in fig. 3(b) of [44]. We remark that the partially flat band can also host correlated quantum states, when the Fermi energy is parked in the flat band region.

Now we are in a position to discuss the periodic strain considered in Sec. III. We take advantage of the gauge redundancy by choosing $A_y = 0$ and $A_x = \frac{-1}{ev_F} t \delta t [\sin(\vec{G}_1 \cdot \vec{r}) - 2 \sin(\vec{G}_2 \cdot \vec{r}) - 2 \sin(\vec{G}_3 \cdot \vec{r})]$. A strain tensor needs to satisfy a compatibility equation for it to correspond to a single valued displacement field [45]. Using the compatibility equation ($\partial_x^2 u_{yy} + \partial_y^2 u_{xx} - 2\partial_{xy}^2 u_{xy} = 0$), we find that the strain field corresponds to displacement field $u_x = -\sqrt{3}u_0 [\cos(\vec{G}_2 \cdot \vec{r}) - \cos(\vec{G}_3 \cdot \vec{r})]$ and $u_y = u_0 \sum_{i=1}^3 \cos(\vec{G}_i \cdot \vec{r})$, where $u_0 = \frac{9eB_0 N_n^2 a^3}{8\pi^2 \hbar \beta}$. Then $-\partial_y A_x(x, y) = B_z$ is the same pseudomagnetic field as in Eq. (10). The Hamiltonian becomes

$$H = v_F (-i\partial_x \sigma_x - i\partial_y \sigma_y - eA_x \sigma_x). \quad (18)$$

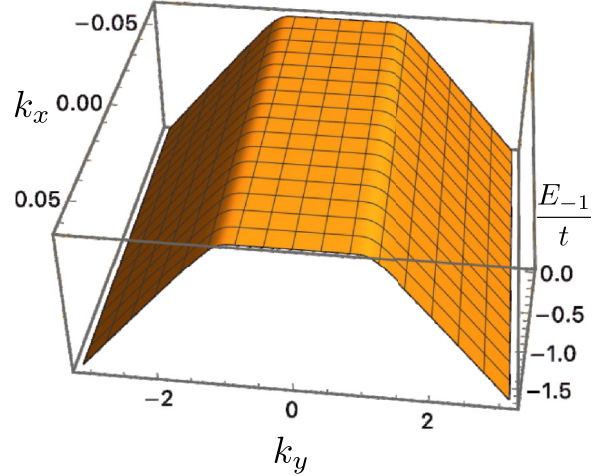


FIG. 9. Band structure of the band -1 of the Hamiltonian of Eq. (17) as a function of k_x and k_y . Here, we set $t = 1$, $\sqrt{3}a = 1$, and $\delta t = 1$.

Assuming that the variation in the y direction is slow and its amplitude is weak, we use the mode expansion:

$$A_{x,m}(y) \equiv \frac{1}{L_x} \int_0^{L_x} A_x(x, y) \exp(-imG_x x) dx, \quad (19)$$

where $G_x = \frac{2\pi}{\sqrt{3}N_n a}$. Plugging Eq. (19) and $\psi(x, y) = \sum_m \exp[i(k_x + mG_x)x] \psi_m(y)$ into the eigenvalue Eq. (18), we get

$$[-i\partial_y \sigma_y + (k_x + mG_x)\sigma_x] \psi_m - \sum_{m'} A_{x,m-m'} \sigma_x \psi_{m'} = E \psi_m. \quad (20)$$

For the $A_x(x, y)$ we use, only $A_{x,0} = \frac{-3B_0 N_n a}{4\pi} \sin(G_1 y)$, $A_{x,-1} = \frac{3B_0 N_n a}{2\pi} \sin(G_2 y)$ and $A_{x,1} = \frac{3B_0 N_n a}{2\pi} \sin(G_3 y)$ are nonzero. We consider the zero mode and set $m = 0$, then we rewrite the Hamiltonian near $E = 0$ as

$$H = -i\partial_y \sigma_y - M(y)\sigma_x, \quad (21)$$

where

$$M(y) = k_x - A_{x,0} - A_{x,-1} A_{x,1} \times \left(\frac{1}{k_x + G_x - A_{x,0}} + \frac{1}{k_x - G_x - A_{x,0}} \right). \quad (22)$$

Plugging in the values of $A_{x,0}$, $A_{x,-1}$, and $A_{x,1}$, we obtain

$$M(y, k_x, \delta t) = \frac{3}{2} a t k_x + t \delta t \sin(G_1 y) - 4t^2 \delta t^2 \sin(G_2 y) \sin(G_3 y) \times \left[\frac{1}{(3/2)at(k_x + G_x) + t\delta t \sin(G_1 y)} + \frac{1}{(3/2)at(k_x - G_x) + t\delta t \sin(G_1 y)} \right]. \quad (23)$$

If we set $t = 1$, we can plot $M(y)$ as a function of y for certain k_x and δt . There are two zeros within one period (see Fig. 10),

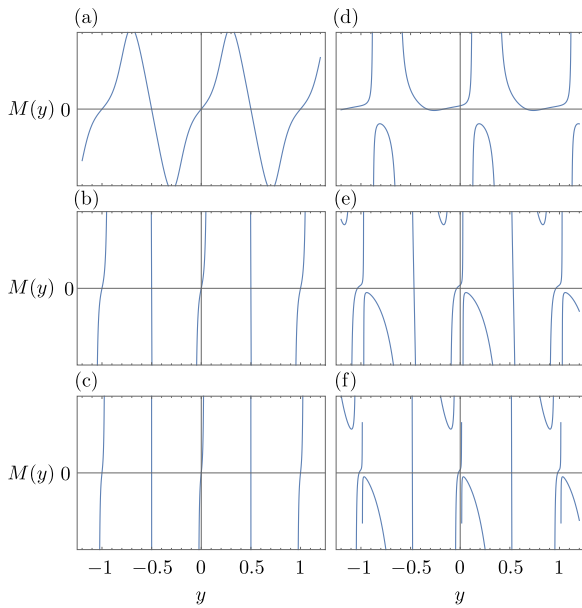


FIG. 10. Zeros of $M(y)$ of the Hamiltonian of Eq. (18) for different k_x and δt . (a)–(c) $k_x = 0$; (d)–(f) $k_x = 0.05$. (a) and (d) $\delta t = 0.05$; (b) and (e) $\delta t = 0.2$; and (c) and (f) $\delta t = 0.4$.

so there should be two flat bands, which is consistent with Fig. 2. Generally, these localized modes hybridize, and therefore, the band cannot be exactly flat. As shown in Fig. 10, for a specific k_x , the slope of $M(y)$ near each zero mode becomes larger as we increase δt , which means the hybridization of the localized mode becomes weaker as we increase δt (recall that the larger the slope at the zeros of $M(y)$, the smaller the spread of the wave function of the localized mode.). As a consequence, the middle two bands become flatter as we increase δt , which qualitatively agree with the bandwidth plot in Fig. 2(b).

VI. DISCUSSION AND CONCLUSIONS

First, we discuss the existing results of the nearly flat band in graphene and bilayer graphene under a periodic potential. Milovanović *et al.* [37] studied band flattening in buckled monolayer graphene numerically by modeling the buckling effect as a pseudomagnetic field. Narrow bands with delocalized electronic dynamics are found. Skurativska *et al.* [46] calculated the electronic structure of single-layer graphene in the presence of periodic adatoms within the framework of density functional theory, where relatively flat bands with fragile topology are reported. The mechanism for the appearance of a nearly flat band in these two works is not clear. In this paper, we unravel the underlying mechanism for the flat band through the JR zero mode. In addition, we provide further characterization of the bands using quantum metric. In Ref. [47], both topological and nontopological flat bands in bilayer graphene under a superlattice potential are demonstrated. The superlattice potential is introduced through spatially modulated electric field, whereas in this paper, the strain modulates the velocity of the Dirac fermion. We would also like to mention closely related systems to a single Dirac fermion on the surface of a topological insu-

lator in the presence of periodic potential, where flat bands and possible correlated states are studied [48,49]. The flat band for Dirac fermions in the presence of a modulated physical magnetic field with a nonzero net magnetic flux is studied in Ref. [50]. The appearance of a flat band due to the relative biasing of one sublattice against other sublattices in bilayer graphene is proposed and verified experimentally in Ref. [51].

Experimentally, periodic strain can be introduced by placing graphene on top of an array of dielectric nanodots. The antisymmetric strain for bilayer graphene may be tricky to implement. Generally, one expects that the strain for different layers can be different when bilayer graphene is placed on a periodic structure. This heterostrain, albeit weak, has been measured experimentally in twisted bilayer graphene devices [13]. Therefore, there exists a strain component that is antisymmetric with respect to the layer degree of freedom. To maximize the antisymmetric component, one can sandwich bilayer graphene with a periodic structure in both the bottom and top. Although we restrict ourselves to periodic strain with C_{3v} symmetry and strain modulated in one direction, the flat bands can also appear for other periodic strain profiles, as can be inferred from the consideration of the JR zero modes. When the strain can be regarded as a gauge field, because of the gauge redundancy, there exist infinitely many strain profiles that produce the same energy spectrum. Therefore, one may take advantage of this gauge redundancy to find a convenient strain profile for experimental realization. As shown in Fig. 5, the band flattens as a function of the strain strength. Compared with twisted bilayer graphene, which requires finetuning of the twist angle to achieve a flat band, strained graphene can achieve a nearly flat band, and the flatness of the band can be improved by continuously tuning the parameters.

As demonstrated in Sec. IV, the response of the system to a strain field can be very different depending on the winding number of the Dirac fermion. For monolayer graphene with Dirac fermion of winding number 1, strain can be modeled as an effective pseudogauge field. For high winding numbers, the Dirac fermion can split in the presence of strain, and the pattern of splitting can be controlled by the symmetry of the strain. In this case, strain generally cannot be modeled as a pseudogauge field. For a higher winding number, which can be realized in multilayer graphene, even richer physics can be expected. Similarly, the many-body instability when electron interactions are included is likely distinct for a Dirac fermion with different winding numbers. The response to strain also depends on the position of the Dirac dispersion in the Brillouin zone [52].

To summarize, we find topological nearly flat bands with a homogeneous distribution of Berry curvature in both monolayer and Bernal-stacked bilayer graphene under periodic strain. Depending on the winding number of the Dirac fermion, the role of strain can either be treated as a pseudogauge field as in monolayer graphene or can be beyond the simple gauge field description as in the case of bilayer graphene. The mechanism of these nearly flat bands can be understood in terms of the Dirac fermion with spatially varying mass terms as in the standard JR model. We further show that the quantum metric of the nearly flat band closely

resembles that for Landau levels. These topological flat bands are a fertile playground for stabilization of interesting many body quantum states. Like other flat band systems [53–57], it is easy to expect a valley polarized state and a fractional Chern insulator at fractional filling of the valley polarized bands. It is also possible to host other non-Abelian topological states due to the nearly ideal quantum metric like Landau levels. We leave the interaction effects for future study.

Note added. During the preparation of this paper, we are aware of work [38] that overlaps in part with the band structure of monolayer graphene under strain in Fig. 2.

ACKNOWLEDGMENTS

We thank Chunli Huang, Jacob Pettine, Houtong Chen, and Filip Ronning for very helpful discussions. The work at LANL (S.-Z.L.) was carried out under the auspices of the U.S. Department of Energy (DOE) National Nuclear Security Administration under Contract No. 89233218CNA000001 through the Laboratory Directed Research and Development Program, was supported by the Center for Nonlinear Studies at LANL (X.W.), and was performed in part at the Center for Integrated Nanotechnologies, an Office of Science User Facility operated for the U.S. DOE Office of Science, under User Proposals No. 2018BU0010 and No. 2018BU0083. This paper was supported in part by the Office of Navy Research Multidisciplinary University Research Initiatives No. N00014-20-1-2479 (X.W., S.S., and K.S.) and Award No. N00014-21-1-2770 (X.W. and K.S.)

and by the Gordon and Betty Moore Foundation Award No. N031710 (K.S.).

APPENDIX: EXPERIMENTAL FEASIBILITY OF NEARLY FLAT BANDS IN MONOLAYER GRAPHENE

To obtain the pseudomagnetic field in Eq. (10), we can put graphene on a substrate which has height profile $h(\mathbf{r}) = h_0 \sum_{i=1}^3 \cos(\vec{G}_i \cdot \mathbf{r} + \frac{\pi}{4})$ [35]. We know

$$t\delta t = \frac{3ev_F B_0 N_n a}{4\pi}, \quad |B_0| \sim (6 \times 10^5 \text{ T}/\text{\AA}^2) \times \frac{h_0^2}{N_n^3},$$

$$\alpha = \frac{\delta t}{(3/2)aG}. \quad (\text{A1})$$

Plugging in the values of e , $v_F = \frac{3}{2}at$, and $a = 1.42 \text{ \AA}$ (a is the bond length of graphene), we obtain

$$|\alpha| \sim \frac{10}{3\pi N_n} (h_0/\text{\AA})^2. \quad (\text{A2})$$

To realize the nearly flat bands at $2.22817 \leq |\alpha| \leq 2.5$ in experiment, we can either utilize nanosphere [58] or nanopillars [59] to achieve the height profile. For nanospheres, we can use 20-nm-diameter nanospheres to achieve a 20 nm superlattice with a period of $N_n = 80$. From fig. 4(e) in Ref. [58], we get an estimate of $h_0 \sim 17.5 \text{ \AA}$ for the 20-nm-diameter nanoparticle case, which corresponds to $|\alpha| = 4.06177$. To exactly access $|\alpha| \sim 2.5$, we just need to use nanospheres with a diameter ~ 15 nm. For nanopillars, we can arrange triangular nanopillars with period 100 nm and height 2.9 nm on a triangular lattice [35].

-
- [1] E. H. Lieb, *Phys. Rev. Lett.* **62**, 1201 (1989).
- [2] K. Sun, Z. Gu, H. Katsura, and S. Das Sarma, *Phys. Rev. Lett.* **106**, 236803 (2011).
- [3] E. Tang, J.-W. Mei, and X.-G. Wen, *Phys. Rev. Lett.* **106**, 236802 (2011).
- [4] T. Neupert, L. Santos, C. Chamon, and C. Mudry, *Phys. Rev. Lett.* **106**, 236804 (2011).
- [5] R. Bistritzer and A. H. MacDonald, *Proc. Natl. Acad. Sci. USA* **108**, 12233 (2011).
- [6] G. Tarnopolsky, A. J. Kruchkov, and A. Vishwanath, *Phys. Rev. Lett.* **122**, 106405 (2019).
- [7] Y. Cao, V. Fatemi, A. Demir, S. Fang, S. L. Tomarken, J. Y. Luo, J. D. Sanchez-Yamagishi, K. Watanabe, T. Taniguchi, E. Kaxiras *et al.*, *Nature (London)* **556**, 80 (2018).
- [8] Y. Cao, V. Fatemi, S. Fang, K. Watanabe, T. Taniguchi, E. Kaxiras, and P. Jarillo-Herrero, *Nature (London)* **556**, 43 (2018).
- [9] X. Lu, P. Stepanov, W. Yang, M. Xie, M. A. Aamir, I. Das, C. Urgell, K. Watanabe, T. Taniguchi, G. Zhang *et al.*, *Nature (London)* **574**, 653 (2019).
- [10] M. Yankowitz, S. Chen, H. Polshyn, Y. Zhang, K. Watanabe, T. Taniguchi, D. Graf, A. F. Young, and C. R. Dean, *Science* **363**, 1059 (2019).
- [11] H. Polshyn, M. Yankowitz, S. Chen, Y. Zhang, K. Watanabe, T. Taniguchi, C. R. Dean, and A. F. Young, *Nat. Phys.* **15**, 1011 (2019).
- [12] Y. Xie, B. Lian, B. Jäck, X. Liu, C.-L. Chiu, K. Watanabe, T. Taniguchi, B. A. Bernevig, and A. Yazdani, *Nature (London)* **572**, 101 (2019).
- [13] A. Kerelsky, L. J. McGilly, D. M. Kennes, L. Xian, M. Yankowitz, S. Chen, K. Watanabe, T. Taniguchi, J. Hone, C. Dean *et al.*, *Nature (London)* **572**, 95 (2019).
- [14] Y. Cao, D. Chowdhury, D. Rodan-Legrain, O. Rubies-Bigorda, K. Watanabe, T. Taniguchi, T. Senthil, and P. Jarillo-Herrero, *Phys. Rev. Lett.* **124**, 076801 (2020).
- [15] Y. Jiang, X. Lai, K. Watanabe, T. Taniguchi, K. Haule, J. Mao, and E. Y. Andrei, *Nature (London)* **573**, 91 (2019).
- [16] Y. Choi, J. Kemmer, Y. Peng, A. Thomson, H. Arora, R. Polski, Y. Zhang, H. Ren, J. Alicea, G. Refael *et al.*, *Nat. Phys.* **15**, 1174 (2019).
- [17] U. Zondiner, A. Rozen, D. Rodan-Legrain, Y. Cao, R. Queiroz, T. Taniguchi, K. Watanabe, Y. Oreg, F. von Oppen, A. Stern *et al.*, *Nature (London)* **582**, 203 (2020).
- [18] D. Wong, K. P. Nuckolls, M. Oh, B. Lian, Y. Xie, S. Jeon, K. Watanabe, T. Taniguchi, B. A. Bernevig, and A. Yazdani, *Nature (London)* **582**, 198 (2020).
- [19] K. P. Nuckolls, M. Oh, D. Wong, B. Lian, K. Watanabe, T. Taniguchi, B. A. Bernevig, and A. Yazdani, *Nature (London)* **588**, 610 (2020).
- [20] M. He, Y. Li, J. Cai, Y. Liu, K. Watanabe, T. Taniguchi, X. Xu, and M. Yankowitz, *Nat. Phys.* **17**, 26 (2021).

- [21] X. Liu, Z. Hao, E. Khalaf, J. Y. Lee, Y. Ronen, H. Yoo, D. Haei Najafabadi, K. Watanabe, T. Taniguchi, A. Vishwanath *et al.*, *Nature (London)* **583**, 221 (2020).
- [22] E. C. Regan, D. Wang, C. Jin, M. I. Bakti Utama, B. Gao, X. Wei, S. Zhao, W. Zhao, Z. Zhang, K. Yumigeta *et al.*, *Nature (London)* **579**, 359 (2020).
- [23] L. Wang, E.-M. Shih, A. Ghiotto, L. Xian, D. A. Rhodes, C. Tan, M. Claassen, D. M. Kennes, Y. Bai, B. Kim *et al.*, *Nat. Mater.* **19**, 861 (2020).
- [24] M. Xie and A. H. MacDonald, *Phys. Rev. Lett.* **124**, 097601 (2020).
- [25] F. Wu and S. Das Sarma, *Phys. Rev. Lett.* **124**, 046403 (2020).
- [26] Y. Su and S.-Z. Lin, *Phys. Rev. Lett.* **125**, 226401 (2020).
- [27] B. Padhi, C. Setty, and P. W. Phillips, *Nano Lett.* **18**, 6175 (2018).
- [28] B. Padhi, R. Chitra, and P. W. Phillips, *Phys. Rev. B* **103**, 125146 (2021).
- [29] B. Padhi and P. W. Phillips, *Phys. Rev. B* **99**, 205141 (2019).
- [30] N. Stefanidis and I. Sodemann, *Phys. Rev. B* **102**, 035158 (2020).
- [31] N. Bultinck, S. Chatterjee, and M. P. Zaletel, *Phys. Rev. Lett.* **124**, 166601 (2020).
- [32] Y. Xu, S. Liu, D. A. Rhodes, K. Watanabe, T. Taniguchi, J. Hone, V. Elser, K. F. Mak, and J. Shan, *Nature (London)* **587**, 214 (2020).
- [33] M. A. H. Vozmediano, M. I. Katsnelson, and F. Guinea, *Phys. Rep.* **496**, 109 (2010).
- [34] N. Levy, S. A. Burke, K. L. Meaker, M. Panlasigui, A. Zettl, F. Guinea, A. H. C. Neto, and M. F. Crommie, *Science* **329**, 544 (2010).
- [35] V. T. Phong and E. J. Mele, *Phys. Rev. Lett.* **128**, 176406 (2022).
- [36] J. Mao, S. P. Milovanović, M. Anđelković, X. Lai, Y. Cao, K. Watanabe, T. Taniguchi, L. Covaci, F. M. Peeters, A. K. Geim *et al.*, *Nature (London)* **584**, 215 (2020).
- [37] S. P. Milovanović, M. Anđelković, L. Covaci, and F. M. Peeters, *Phys. Rev. B* **102**, 245427 (2020).
- [38] Q. Gao, J. Dong, P. Ledwith, D. Parker, and E. Khalaf, *Phys. Rev. Lett.* **131**, 096401 (2023).
- [39] M. T. Mahmud, D. Zhai, and N. Sandler, *Nano Lett.* **23**, 7725 (2023).
- [40] N. Regnault, Y. Xu, M.-R. Li, D.-S. Ma, M. Jovanovic, A. Yazdani, S. S. P. Parkin, C. Felser, L. M. Schoop, N. P. Ong *et al.*, *Nature (London)* **603**, 824 (2022).
- [41] H. Suzuura and T. Ando, *Phys. Rev. B* **65**, 235412 (2002).
- [42] Y. Aharonov and A. Casher, *Phys. Rev. A* **19**, 2461 (1979).
- [43] R. Jackiw and C. Rebbi, *Phys. Rev. D* **13**, 3398 (1976).
- [44] L. Meng, W.-Y. He, H. Zheng, M. Liu, H. Yan, W. Yan, Z.-D. Chu, K. Bai, R.-F. Dou, Y. Zhang *et al.*, *Phys. Rev. B* **87**, 205405 (2013).
- [45] J. R. Barber, *Elasticity, Solid Mechanics and Its Applications*, Vol. 172 (Springer, New York, 2002).
- [46] A. Skurativska, S. S. Tsirkin, F. D. Natterer, T. Neupert, and M. H. Fischer, *Phys. Rev. Res.* **3**, L032003 (2021).
- [47] S. A. A. Ghorashi, A. Dunbrack, A. Abouelkomsan, J. Sun, X. Du, and J. Cano, *Phys. Rev. Lett.* **130**, 196201 (2023).
- [48] T. Wang, N. F. Q. Yuan, and L. Fu, *Phys. Rev. X* **11**, 021024 (2021).
- [49] J. Cano, S. Fang, J. H. Pixley, and J. H. Wilson, *Phys. Rev. B* **103**, 155157 (2021).
- [50] J. Dong, J. Wang, and L. Fu, [arXiv:2208.10516](https://arxiv.org/abs/2208.10516) [cond-mat.mes-hall].
- [51] D. Marchenko, D. Evtushinsky, E. Golias, A. Varykhalov, T. Seyller, and O. Rader, *Sci. Adv.* **4**, eaau0059 (2018).
- [52] X. Wan, S. Sarkar, S.-Z. Lin, and K. Sun, *Phys. Rev. Lett.* **130**, 216401 (2023).
- [53] P. J. Ledwith, G. Tarnopolsky, E. Khalaf, and A. Vishwanath, *Phys. Rev. Res.* **2**, 023237 (2020).
- [54] C. Repellin and T. Senthil, *Phys. Rev. Res.* **2**, 023238 (2020).
- [55] Z. Liu, A. Abouelkomsan, and E. J. Bergholtz, *Phys. Rev. Lett.* **126**, 026801 (2021).
- [56] H. Li, U. Kumar, K. Sun, and S.-Z. Lin, *Phys. Rev. Res.* **3**, L032070 (2021).
- [57] Y. Xie, A. T. Pierce, J. M. Park, D. E. Parker, E. Khalaf, P. Ledwith, Y. Cao, S. H. Lee, S. Chen, P. R. Forrester *et al.*, *Nature (London)* **600**, 439 (2021).
- [58] Y. Zhang, M. Heiranian, B. Janicek, Z. Budrikis, S. Zapperi, P. Y. Huang, H. T. Johnson, N. R. Aluru, J. W. Lyding, and N. Mason, *Nano Lett.* **18**, 2098 (2018).
- [59] Y. Jiang, J. Mao, J. Duan, X. Lai, K. Watanabe, T. Taniguchi, and E. Y. Andrei, *Nano Lett.* **17**, 2839 (2017).